MATERIALS CHEMISTRY
FRONTIERS

RESEARCH ARTICLE

View Article Online
View Journal | View Issue

Cite this: *Mater. Chem. Front.*, 2019, **3**, 2032

1T-phase MoS_2 quantum dots as a superior co-catalyst to Pt decorated on carbon nitride nanorods for photocatalytic hydrogen evolution from water†

Zhangqian Liang, Yichen Guo, Yanjun Xue, Hongzhi Cui * and Jian Tian *

Received 10th April 2019,
Accepted 4th June 2019

DOI: 10.1039/c9qm00223e

rsc.li/frontiers-materials

Molybdenum disulfide (MoS_2) has been confirmed to be a promising non-precious-metal co-catalyst for photocatalytic hydrogen (H_2) evolution; however, its low-density of active sites and poor electron transfer efficiency have essentially limited its photocatalytic properties. Here we report that 1T-MoS_2 quantum dots (QDs) can exceed the performance of noble metals like Pt as co-catalysts in assisting photocatalytic H_2 evolution upon forming a heterostructure with C_3N_4 nanorods (denoted as 1T-MoS_2@C_3N_4 NRs). The presence of 1T-MoS_2 QDs is found to improve light harvesting, enhance electronic conductivity as well as boost the density of active sites, resulting in an excellent light absorption range up to the near-infrared (NIR) region and a highly efficient spatial charge separation and transfer process. As a result, the optimized 1T-MoS_2@C_3N_4 NR composite (5.0 wt%) exhibits an extraordinary photocatalytic H_2 production rate of 565 μmol h^{-1} g^{-1} under simulated solar light irradiation, obviously higher than that of noble metal Pt loaded C_3N_4 NRs (318 μmol h^{-1} g^{-1}). Moreover, the 1T-MoS_2@C_3N_4 NR composites exhibit good stability in the cyclic runs for photocatalytic H_2 production. This study indicates that the highly active MoS_2 as a co-catalyst is highly promising as a substitute for Pt for photocatalytic H_2 evolution.

1. Introduction

Due to the emerging energy crisis and global environmental awareness,[1–3] the conversion of solar energy into perfect hydrogen (H_2) energy *via* photocatalytic water splitting using semiconductors as catalysts has attracted significant attention.[4–7] Hydrogen is considered as an ideal, clean and sustainable candidate to replace exhaustible fossil fuels.[8–11] Until now, a rich variety of semiconductor materials have been explored as photocatalysts for hydrogen production.[12–15] As a promising semiconductor photocatalyst, C_3N_4 nanorods (NRs) exhibit a suitable band gap (about 1.38 eV), broader visible-light absorption range than g-C_3N_4 nanosheets (about 2.47 eV) and a negative conduction band edge potential (below the reduction potential of H_2O/H_2) for splitting water.[16,17] However, bare C_3N_4 NRs show extremely low activity for the photocatalytic H_2 evolution reaction due to the rapid recombination of photogenerated electrons and holes and lack of active sites for photocatalysis.[18] Integration of co-catalysts, such as noble metals Au and Pt, into C_3N_4 NRs has proven to be an effective way for suppressing electron–hole recombination and accelerating photocatalytic H_2 evolution.[19] However, the scale-up application of the commonly used noble metal co-catalysts is still largely restricted due to their low abundance and high cost.[19,20] Therefore, there is in an urgent need to seek noble-metal free alternative co-catalysts compounded with C_3N_4 NRs for synthesizing C_3N_4 NR-based heterostructures with significantly enhanced photocatalytic activity.

As a typical layered transition metal sulfide, molybdenum disulfide (MoS_2), with a sandwich structure of three stacked atomic layers (S–Mo–S), has been considered a promising alternative for noble-metal co-catalysts due to its abundance and low cost.[21–24] MoS_2 has been designed with various nanostructures, such as nanoparticles,[25,26] nanowires,[27,28] nanoflowers,[29,30] nanosheets,[31,32] and quantum dots (QDs).[33,34] Interestingly, MoS_2 QDs have attracted more significant attention due to their better solubility in aqueous solvents and more edge atoms compared with other MoS_2 nanostructures or bulk-MoS_2.[35] It is well known that MoS_2 usually has two phase structures, including a trigonal phase (1T-MoS_2) and a hexagonal phase (2H-MoS_2).[36,37] Natural MoS_2 usually exists in the stable 2H phase, showing semiconducting properties with a tunable bandgap of 1.3–1.9 eV.[21] However, the inherent semiconducting character of 2H-MoS_2 with a low density of active sites and poor conductivity restricts its catalytic performance.[1] As reported previously,[38] 1T-MoS_2 offers dense active sites containing catalytically active edges and basal planes,

School of Materials Science and Engineering, Shandong University of Science and Technology, Qingdao, 266590, China. E-mail: cuihongzhi1965@163.com, jiantian@sdust.edu.cn

† Electronic supplementary information (ESI) available. See DOI: 10.1039/c9qm00223e

while 2H-MoS_2 only possesses edge sites. Besides, compared to 2H-MoS_2, the metallic 1T-MoS_2 displays excellent conductivity characteristics at ambient temperature, making it suitable as a co-catalyst to accept the electrons for H_2 evolution.[39]

This study aims to prepare highly active MoS_2 substituting for noble metal Pt for photocatalytic H_2 evolution and clearly certify the electron transfer process between C_3N_4 and MoS_2. Herein, we prepare 1T-MoS_2 QD decorated C_3N_4 NRs (1T-MoS_2@C_3N_4 NRs) by a sonication-assisted hydrothermal method. The obtained 1T-MoS_2@C_3N_4 NR composites exhibit a broad visible and near-infrared (NIR) light absorption range, excellent photocurrent response and charge transfer activity. The 1T-MoS_2@C_3N_4 NR composite with optimal 1T-MoS_2 QD loading of 5.0 wt% exhibits a drastically enhanced photocatalytic H_2 evolution rate of 565 μmol h^{-1} g^{-1}, which is almost 1.8 times higher than that of Pt@C_3N_4 NRs (318 μmol h^{-1} g^{-1}) under simulated solar light irradiation, as well as good stability in photocatalytic cyclic runs. The 1T-MoS_2 QDs apparently show metallic characteristics like Pt, and a series of experimental studies have proven the photogenerated electron transfer process and photocatalytic mechanism.

2. Experimental section

2.1. Synthesis of C_3N_4 nanorods (NRs)

In a typical procedure (Scheme 1), 2.7675 g of 1,3,5-trichlorotriazine and 0.9459 g of melamine powder were dissolved in 60 mL of acetonitrile. The mixture was stirred for 12 h, and then put into a 100 mL Teflon-lined stainless steel autoclave, which was sealed and maintained at 180 °C for 96 h. After heating at a certain temperature, the autoclave was allowed to cool to room temperature naturally. The obtained product was sequentially washed with acetonitrile, distilled water and absolute ethanol several times to remove residual impurities and then the resulting powder was dried at 60 °C for 12 h to get the final products.

2.2. Preparation of 1T-MoS_2 quantum dots (QDs)

1T-MoS_2 QDs were prepared by a simple hydrothermal method (Scheme 2). Specifically, 0.4 g of $Na_2MoO_4{\cdot}2H_2O$ and 0.38 g of $C_{14}H_{14}S_2$ were dissolved in 30 mL of deionized water and 30 mL of ethanol with sonication for 30 min, respectively. Then, $C_{14}H_{14}S_2$ solution was added to the $Na_2MoO_4{\cdot}2H_2O$ solution. After sonication for 30 min, the mixture was then transferred to a 100 mL Teflon-lined stainless steel autoclave and heated at 180 °C for 20 h. After the autoclave was cooled to room temperature naturally, the light yellow supernatant was discarded and then

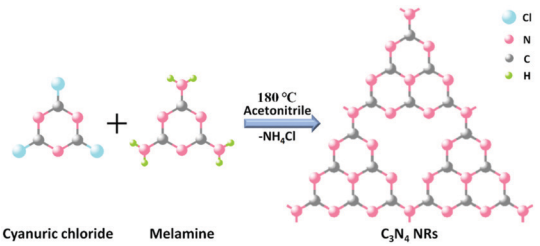

Scheme 1 Schematic illustration of the C_3N_4 NR reaction.

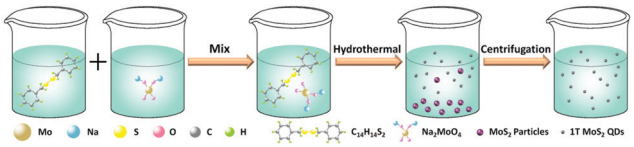

Scheme 2 Schematic illustration of the synthetic route for 1T-MoS_2 QDs through a hydrothermal technique.

30 mL of deionized water was added to disperse the black product. The resulting suspension was then centrifuged for 90 min at 12 000 rpm to separate the supernatant and sediment, and the supernatant was 1T-MoS_2 QDs. In order to determine the concentration of the 1T-MoS_2 QD solution, the supernatant was treated by freeze drying to obtain a powder. Therefore, the concentration of the as-prepared 1T-MoS_2 QD solution was determined to be about 0.2 mg mL^{-1} in terms of the measured weight and the volume of solution before freeze drying.

2.3. Preparation of 1T-MoS_2@C_3N_4 NR composites

200 mg of C_3N_4 NRs and 50 mL (0.2 mg mL^{-1}) of the as-prepared 1T-MoS_2 QD solution were mixed and then sonicated for over 2 h. Subsequently, the obtained mixture was centrifuged and dried at 60 °C to gain the target product (1T-MoS_2@C_3N_4 NRs with 1T-MoS_2 QD loading of 5.0 wt%). Similarly, a series of hybrid catalysts, including 1T-MoS_2@C_3N_4 NRs with 1T-MoS_2 QD loading of 0.5 wt%, 1.0 wt%, 3.0 wt% and 7.0 wt%, were obtained by adjusting the volume of the 1T-MoS_2 QD solution as 5, 10, 30 and 70 mL, respectively.

2.4. Characterization

The synthesized products were characterized by X-ray diffraction (XRD, D/Max 2500PC Rigaku, Japan) utilizing a Cu Kα (λ = 1.5418 Å) radiation source operated at 40 kV at a scan rate of 4° min^{-1}. The nanostructure and surface characteristics of the products were studied on a high-resolution scanning electron microscope (FESEM, FEI Nova Nanosem 450, USA). The morphology and crystal structure of the samples were characterized by transmission electron microscopy (TEM) and high resolution TEM (HRTEM) (JEOL JEM 2100F) with an accelerating voltage of 200 kV, and their composition was examined using energy-dispersive X-ray spectroscopy (EDS) attached to the TEM instrument. X-ray photoelectron spectroscopy (XPS) was carried out with a Thermo ESCALAB 250XI spectrometer using Al Kα radiation at a voltage of 1486.6 eV and calibrated with the C 1s binding energy of 284.8 eV. The XPS results were deconvoluted with XPSPEAK software. The UV-vis-NIR diffuse reflectance spectra (DRS) of the samples were recorded on a UV-vis-NIR spectrophotometer (Hitachi UV-3101) with an integrating sphere attachment within the 200–2000 nm range and with $BaSO_4$ as the reflectance standard. The Brunauer–Emmett–Teller (BET) specific surface area measurements were carried out by N_2 adsorption at 77 K using a Micromeritics ASAP2020 nitrogen adsorption–desorption apparatus with prior out gassing of the sample overnight at 120 °C under a primary vacuum. Raman spectra were measured with solid samples using a HORIBA LabRAM HR Evolution Raman microscope. Transient photoluminescence curves of the as-prepared samples were obtained on a FLS980 Series fluorescence lifetime spectrophotometer.

2.5. Photoelectrochemical measurements

The photocurrent response and electrochemical impedance of the samples were tested by using an electrochemical workstation (Shanghai Chenhua CHI660D) in a three-electrode system, in which the sample electrode was used as the photocathode, Ag/AgCl as the reference electrode, a Pt wire as the counter electrode, and 0.5 M Na_2SO_4 aqueous solution as the electrolyte. The working electrodes were prepared as follows: 5 mg of the photocatalyst (1T-MoS_2@C_3N_4 NRs composites) and 1 mg of ethyl cellulose were dispersed into a solution containing 250 μL of ethanol and 250 μL of terpineol by 60 min sonication to prepare a homogeneous slurry. Then, 250 μL of the slurry was dropped onto pretreated stannic oxide (FTO) conductive glass with an exposed area of 4.0 cm^2 (2 cm × 2 cm). A 500 W Xe arc lamp equipped with an AM-1.5 filter was adopted as the light source.

2.6. Photocatalytic H_2 evolution

Photocatalytic H_2 production experiments were carried out in an outer irradiation type photoreactor (100 mL quartz glass) in a N_2 environment. 20 mg of the 1T-MoS_2@C_3N_4 NR composite photocatalyst was dispersed with mechanical stirring in 100 mL of an aqueous solution containing 20 vol% triethanolamine for further photocatalytic H_2 production experiments. Before irradiation, the photocatalytic system was thoroughly degassed to remove air by bubbling N_2 for 20 min. The irradiation light source used in this study was a 300 W Xe arc lamp (CELHXF300, Beijing China Education Au-light Co., Ltd), which was equipped with an AM-1.5 filter. The evolved gas was analyzed using a gas chromatograph (Techcomp GC-7920) equipped with a thermal conductivity detector (TCD). The apparent quantum efficiency (AQE) was measured under similar photocatalytic reaction conditions except that a 300 W Xe arc lamp with an AM-1.5 filter was used as the light source. The focused intensity for the 300 W Xe arc lamp with the AM-1.5 filter was *ca.* 4601.7 W m^{-2}. The apparent quantum efficiency (AQE) was measured and calculated according to the equation:

$$\mathrm{AQE} = \frac{\text{number of reacted electrons}}{\text{number of incident photons}} \times 100$$

$$= \frac{\text{number of evolved } H_2 \text{ molecules} \times 2}{\text{number of incident photons}} \times 100\%$$

3. Results and discussion

Firstly, the C_3N_4 NRs were prepared by solvothermally treating cyanuric chloride and melamine in acetonitrile solution at 180 °C for 96 h. Under these conditions, the C_3N_4 frameworks could be formed due to the condensation of triazine tectons from cyanuric chloride and melamine, accompanied by the release of NH_4Cl (Scheme 1). Then, 1T-MoS_2 QDs were fabricated by a simple hydrothermal method (Scheme 2). The obtained 1T-MoS_2 QDs not only act as electron acceptors with high electrical conductivity, but also offer abundant reaction sites for H_2 evolution. Ultimately, 1T-MoS_2@C_3N_4 NR composite photocatalysts were prepared *via* ultrasonic mixing; in this process, 1T-MoS_2 QDs were perfectly decorated on the surface of

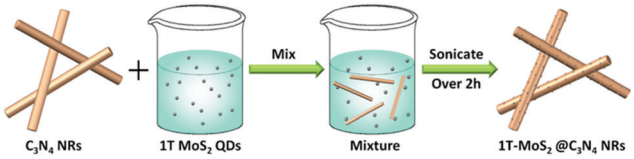

Scheme 3 Schematic illustration for the formation of 1T-MoS_2@C_3N_4 NR composites.

C_3N_4 NRs and offer dense active sites containing catalytically active edges and basal planes, just as schematically shown in Scheme 3.

The phases of C_3N_4 NRs and 1T-MoS_2@C_3N_4 NR composites with varying loadings of 1T-MoS_2 QDs (0.5, 1.0, 3.0, 5.0 and 7.0 wt%) were investigated by the X-ray diffraction (XRD) patterns (Fig. 1). For comparison, g-C_3N_4 was obtained by the thermal polymerization of urea. As shown in Fig. S1 (ESI†), g-C_3N_4 exhibits two peaks located at 13.0° and 27.5°, which can be well indexed to the (100) and (002) planes of g-C_3N_4, respectively.[40,41] Compared with g-C_3N_4, C_3N_4 NRs only display one characteristic diffraction peak located at 27.5°, which corresponds to the (002) plane of g-C_3N_4 due to the interlayer stacking of the conjugated aromatic systems.[42] After 1T-MoS_2 QD decoration, all 1T-MoS_2@C_3N_4 NR samples exhibit similar diffraction patterns and show no XRD peak shift compared to pure C_3N_4 NRs. This indicates that the C_3N_4 NR is the basic structure of the obtained samples, and its structure does not change after 1T-MoS_2 QD loading.[42] It is obvious that no diffraction peaks of 1T-MoS_2 QDs can be observed even for 1T-MoS_2@C_3N_4 NRs (7.0 wt%) due to the low concentration and/or low crystallinity of 1T-MoS_2 in the composites.[43,44]

The elemental composition and chemical status of 1T-MoS_2@C_3N_4 NR composites were further investigated by X-ray photoelectron spectroscopy (XPS). The XPS survey spectrum (Fig. S2, ESI†) indicates that the 1T-MoS_2@C_3N_4 NR composites are composed of C, N, Mo and S elements. In addition, the O 1s peak can also be found, due to the surface absorption and oxidation during the preparation process.[45] To further analyze the 1T-MoS_2@C_3N_4 NR composites, the high-resolution spectra for C 1s, N 1s Mo 3d and S 2p of the 1T-MoS_2@C_3N_4 NR

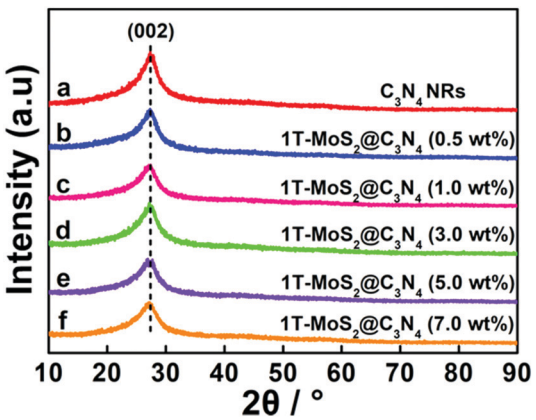

Fig. 1 XRD patterns of C_3N_4 NRs and 1T-MoS_2@C_3N_4 NR composites containing different amounts of 1T-MoS_2 QDs (0.5, 1.0, 3.0, 5.0 and 7.0 wt%).

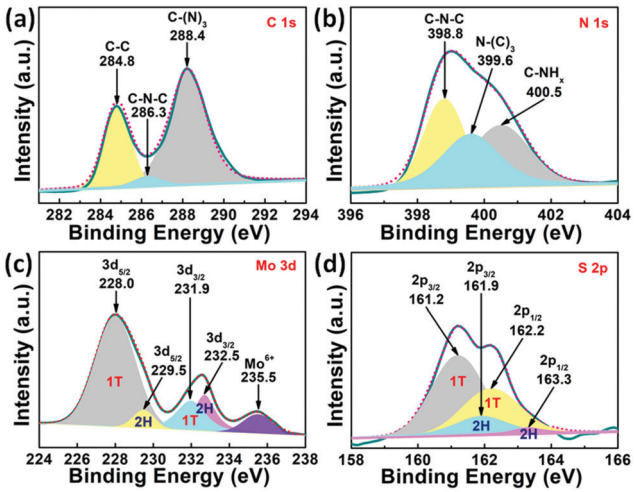

Fig. 2 High-resolution peak-fitting XPS spectra of (a) C 1s, (b) N 1s, (c) Mo 3d and (d) S 2p of 1T-MoS_2@C_3N_4 NR composites (5.0 wt%).

composites are depicted (Fig. 2). The C 1s spectrum (Fig. 2a) of the samples shows three peaks at 284.8, 286.3 and 288.4 eV, which can be attributed to the carbon nitride matrix group (C–C), the sp^2-hybridized carbon atoms bonded to nitrogen atom in the aromatic ring group (C–N–C) and the sp^2-hybridized carbon atoms bonded to three nitrogen atoms in the aromatic ring attached to the NH_2 group (C–$(N)_3$), respectively.[46,47] The N 1 s spectrum (Fig. 2b) can be fitted into three peaks at 398.8, 399.6 and 400.5 eV, which arise from the sp^2-hybridized nitrogen atom (C–N–C), sp^3-hybridized nitrogen atom (N–$(C)_3$) and amino groups carrying hydrogen (C–NH_x), respectively.[16,48] To better illustrate the existence of 1T-MoS_2, the Mo 3d and S 2p XPS spectra of the 1T-MoS_2@C_3N_4 NR composites are given in Fig. 2c and d. The Mo 3d spectrum (Fig. 2c) can be resolved into five peaks. The two small peaks located at 229.5 eV (Mo $3d_{5/2}$) and 232.5 eV (Mo $3d_{3/2}$) indicate the 4+ oxidation state of 2H-phase MoS_2, and the main peaks at 228.0 and 231.9 eV suggest the formation of 1T-phase MoS_2.[49,50] The peak located at 235.5 eV was assigned to Mo^{6+}, probably owing to the oxidation of 1T-MoS_2@C_3N_4 NRs by the exposure to air. Fig. 2d shows the S 2p spectrum, in which the main two peaks at 161.2 eV (S $2p_{3/2}$) and 162.2 eV (S $2p_{1/2}$) represent the 1T-phase MoS_2, and the two small peaks at 161.9 eV (S $2p_{3/2}$) and 163.3 eV (S $2p_{1/2}$) indicate the 2H-phase MoS_2.[49,50] The concentration of the 1T phase in the 1T-MoS_2@C_3N_4 NR composites is approximately calculated to be ~79%, which indicates the predominance of the 1T phase over its 2H counterpart. The above results further confirm the existence of C_3N_4 and 1T-MoS_2 in 1T-MoS_2@C_3N_4 NR samples. The vibrational properties of the prepared C_3N_4 NRs and 1T-MoS_2@C_3N_4 NR composites (5.0 wt%) were determined by Raman spectroscopy. As can be seen in Fig. S3 (ESI†), the band at 978 cm^{-1} corresponds to the stretching vibration of the CN heterocycle in the g-C_3N_4 structure.[51] The band at 740 cm^{-1} is also ascribed to g-C_3N_4, which appears in both spectra. No peaks ascribed to 1T-MoS_2 QDs can be detected in the 1T-MoS_2@C_3N_4 NRs (5.0 wt%), due to the low content of MoS_2 in the hybrid. This result is consistent with the XRD data as shown in Fig. 1.

The morphology and size of C_3N_4 NRs and 1T-MoS_2@C_3N_4 NR composites were investigated by scanning electron microscopy (SEM). Obviously, the C_3N_4 sample exhibits a rod-like structure with a length of 300–500 nm (Fig. 3a). Subsequently, the surface decoration of C_3N_4 NRs with 1T-MoS_2 QDs was carried out by sonication of the C_3N_4 NRs in an aqueous solution of 1T-MoS_2 QDs for over 2 h. In this process, 1T-MoS_2 QDs could be absorbed on the surface of C_3N_4 NRs, resulting in the assembly of 1T-MoS_2 QDs on C_3N_4 NRs (Scheme 3). The obtained 1T-MoS_2@C_3N_4 NR composites still retained the rod-shaped structure (Fig. 3b). 1T-MoS_2 QDs were difficult to discern through SEM due to their very small size.

In order to further visualize the morphology and microstructure of the as-prepared pure 1T-MoS_2 QDs and 1T-MoS_2@C_3N_4 NR composites, TEM images were employed (Fig. 4 and 5). Obviously, Fig. 4a reveals that pure 1T-MoS_2 QDs are distributed homogeneously without apparent aggregation, which possess well-dispersed ultrasmall particles of size about 2–3 nm. From the HRTEM image (Fig. 4b) of 1T-MoS_2 QDs, no typical (002) lattice plane of crystalline MoS_2 is observed, indicating that 1T-MoS_2 QDs contain only a single layer or very few layers.[52] The atomic force microscopy (AFM) image shown in Fig. S4 (ESI†) also confirms the formation of the 1T-MoS_2 QDs with good dispersion. Furthermore, the 1T-phase MoS_2 can be clearly visualized (inset in Fig. 4b), evidently displaying the trigonal lattice areas (octahedral coordination) of the 1T phase of MoS_2 QDs.[50,53] As displayed in Fig. 5a, the 1T-MoS_2@C_3N_4 NR composites exhibit a 1D rod-shaped morphology. However, plenty of black dot-like structures (the regions enclosed by the red circles) are seen decorating the nanorod with a diameter of several nanometers (Fig. 5b). A closer inspection of the TEM image

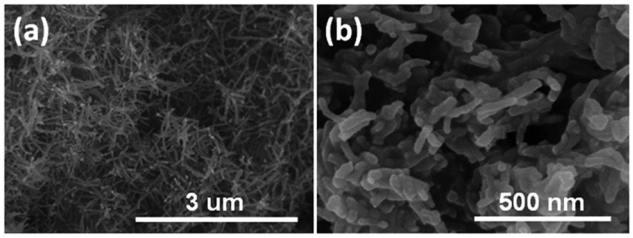

Fig. 3 SEM images of (a) C_3N_4 NRs and (b) 1T-MoS_2@C_3N_4 NR composites (5.0 wt%).

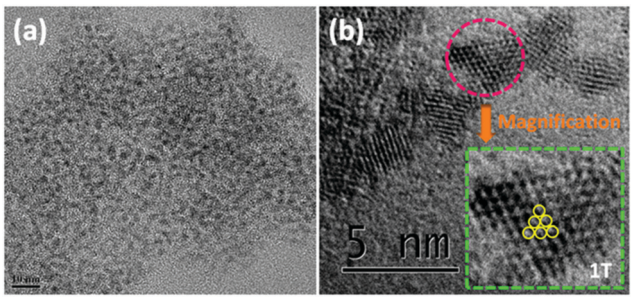

Fig. 4 (a) TEM images and (b) HRTEM image of 1T-MoS_2 QDs (the inset shows the magnification of the region enclosed by the pink circle).

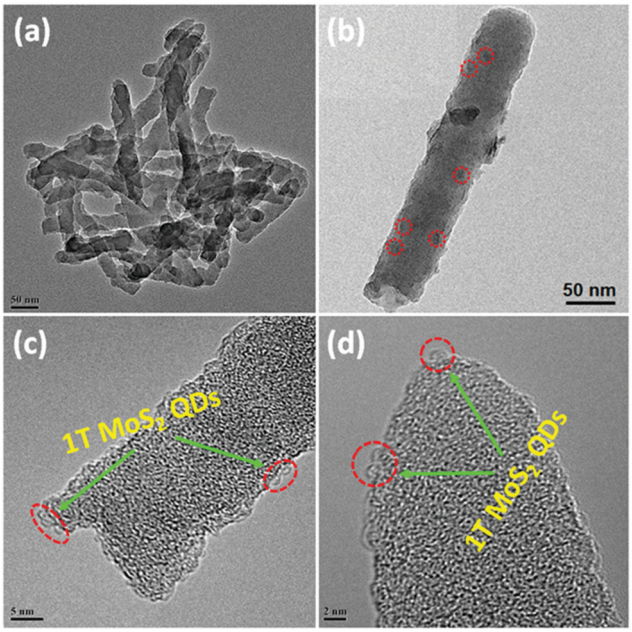

Fig. 5 TEM image of 1T-MoS_2@C_3N_4 NR composites (5.0 wt%).

(Fig. 5c and d) indicates that these nanodots (1T-MoS_2 QDs) are closely attached on the surface of the nanorod. Such a heterostructure with close contact interfaces ensures the fast separation and transfer of charge carriers across the interfaces. Moreover, the EDS mapping (Fig. 6) analysis of 1T-MoS_2@C_3N_4 NR composites displays the uniform distribution of C, N, Mo and S, further confirming that 1T-MoS_2 QDs are successfully loaded on the surface of C_3N_4 NRs.

To determine the surface area of the as-synthesized samples, the N_2 adsorption–desorption isotherms were measured for the samples. The nitrogen adsorption–desorption isotherms and the corresponding pore size distribution curves of the samples are shown in Fig. S5 (ESI†), and the specific surface areas of the samples are listed in Table S1 (ESI†). The N_2 adsorption–desorption isotherms of all the samples are typical Langmuir type IV isotherms with a typical H_3 hysteresis loop at high pressure, indicating the presence of mesopores in all samples.[54,55] The pore size distribution curves (Fig. S5b–f, ESI† inset) reveal that the pore size diameter of the 1T-MoS_2@C_3N_4 NR composites is about 2 nm, while the pore size diameter of pure C_3N_4 NRs is about 4 nm (Fig. S5a, ESI† inset). Besides, the results show that the 1T-MoS_2@C_3N_4 NR composites containing different amounts of 1T-MoS_2 QDs have similar specific surface areas (Table S1, ESI†). Thus, the effect of the BET surface area on the hydrogen evolution activity of the 1T-MoS_2@C_3N_4 NR composites is uncertain in this work.

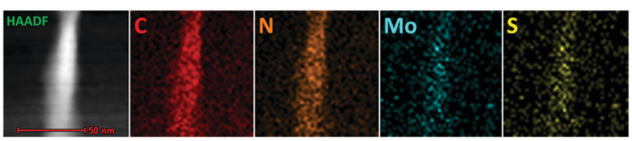

Fig. 6 Selected HAADF image and corresponding EDS elemental mappings of 1T-MoS_2@C_3N_4 NR composites (5.0 wt%).

The optical properties of the samples were measured by UV-vis-NIR diffuse reflectance spectroscopy (DRS) (Fig. 7 and Fig. S6a, ESI†). As shown in Fig. S6a (ESI†), g-C_3N_4 nanosheets exhibit a short-wavelength absorption with an edge at ~470 nm. For the C_3N_4 NR sample, it exhibits a wide photoabsorption range from the UV to visible region with an absorption edge at ~754 nm, indicating a large redshift compared with that of pure g-C_3N_4 (~470 nm). The UV-vis-NIR absorption spectrum of 1T-MoS_2 QDs gives a smooth line without any obvious absorption band (Fig. S7, ESI†), confirming the metallic characteristics of 1T-MoS_2 QDs. Furthermore, it is obvious that loading the 1T-MoS_2 QD co-catalysts onto the surface of C_3N_4 NRs can broaden the absorption range to the NIR light region (Fig. 7). Importantly, the 1T-MoS_2@C_3N_4 NR composites (5.0 wt%) display stronger optical absorption with an edge at ~850 nm, indicating a large red-shift compared with that of C_3N_4 NRs and 1T-MoS_2@C_3N_4 NR composites containing other amounts of 1T-MoS_2 QDs (0.5, 1.0, 3.0 and 7.0 wt%). Thus, the enhanced light absorption of 1T-MoS_2@C_3N_4 NR composites is favorable to produce more photo-generated electrons and holes, which is in turn beneficial to the photocatalytic HER activity.[56] Furthermore, the band gap energy of g-C_3N_4 and C_3N_4 NRs could be computed from the formula $(\alpha h\nu)^{1/2} \propto h\nu - E_g$, where α, h, ν, and E_g are the absorption coefficient, Planck's constant, light frequency, and band gap energy, respectively. Then the estimated E_g of g-C_3N_4 and C_3N_4 NRs is 2.47 and 1.38 eV, respectively (Fig. S6b, ESI†).

We further tested the photoexcited charge carrier lifetimes of pure C_3N_4 NRs and 1T-MoS_2@C_3N_4 NR composites by using time-resolved fluorescence decay spectroscopy. As shown in Fig. 8, by fitting the fluorescence lifetime decay curve, we conclude that both pure C_3N_4 NRs and 1T-MoS_2@C_3N_4 NR composites show single exponential decay. The intensity-average lifetime (τ) of pure C_3N_4 NRs is 0.1545 ns, which is lower than that of the 1T-MoS_2@C_3N_4 NR composites (0.3585 ns). The extension of the trapped carrier lifetimes in 1T-MoS_2@C_3N_4 NR composites indicates the advantages of surface decoration of C_3N_4 NRs by 1T-MoS_2 QDs, which promotes electron–hole separation and hinders their efficient recombination.

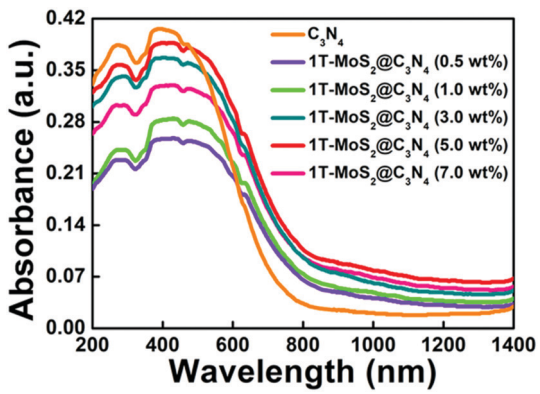

Fig. 7 UV-vis-NIR light absorption spectra of C_3N_4 NRs and 1T-MoS_2@C_3N_4 NR composites containing different amounts of 1T-MoS_2 QDs (0.5, 1.0, 3.0, 5.0 and 7.0 wt%).

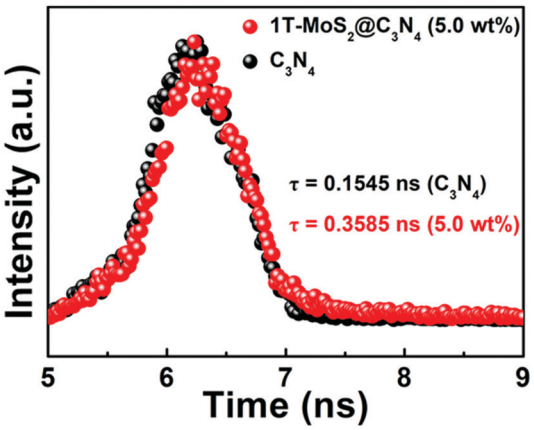

Fig. 8 Luminescence decay curves of pure C_3N_4 NRs and 1T-MoS_2@C_3N_4 NR composites (5.0 wt%).

To gain deep insights into the charge transfer behaviors in the 1T-MoS_2@C_3N_4 NR composites, the photocurrent responses were studied and electrochemical impedance spectroscopy (EIS) was carried out. Fig. 9a shows the periodic on/off photocurrent response of all samples when irradiated under solar light. It can be seen that all the samples show an immediate rise in the photocurrent response when the light is on. In contrast, the photocurrent rapidly decreases to zero when the light is turned off. The on–off cycles of photocurrent are reproducible, which indicates that the photogenerated electrons are transferred to the back contact across the samples to form the photocurrent under light irradiation.[57] The pure C_3N_4 NR electrode generates a relatively low photocurrent density of 0.019 μA cm^{-2}. The photocurrent response curves (Fig. 9a) show an increased current density in all 1T-MoS_2@C_3N_4 NR samples as compared with pure C_3N_4 NRs, indicating a noticeable improvement of the electron–hole separation efficiency by the introduction of 1T MoS_2 QD co-catalysts.[56] The 1T-MoS_2@C_3N_4 NR composite (5.0 wt%) electrode shows the highest photocurrent density of 0.108 μA cm^{-2}, which is about 5.7 times higher than that of a bare C_3N_4 NR electrode. On the one hand, 1T-MoS_2@C_3N_4 NR composites (5.0 wt%) have a wider absorption range and stronger photoabsorption ability, resulting in more photogenerated carriers. On the other hand, 1T-MoS_2 QDs can act as electron acceptors to capture photo-generated electrons before they recombine with holes, leading to more effective separation of electron–hole pairs. The EIS measurement is also an effective approach to study the charge transfer process. In general, a smaller arc radius on an EIS Nyquist plot means a smaller charge-transfer resistance on the electrode surface and a higher separation efficiency of electron–hole pairs.[58] As illustrated in Fig. 9b, the order of arc size for the samples under solar light irradiation is 1T-MoS_2@C_3N_4 NR composites (5.0 wt%) < 1T-MoS_2@C_3N_4 NR composites (3.0 wt%) < 1T-MoS_2@C_3N_4 NR composites (7.0 wt%) < 1T-MoS_2@C_3N_4 NR composites (1.0 wt%) < 1T-MoS_2@C_3N_4 NR composites (0.5 wt%) < pure C_3N_4 NRs, suggesting that the 1T-MoS_2@C_3N_4 NR composites (5.0 wt%) display the most effective separation of photogenerated charges. Apparently, this is in good agreement with luminescence decay and photocurrent results, validating that the 1T-MoS_2@C_3N_4 NR composites would obviously improve the charge transfer rate. Note that the higher interfacial charge transfer ability of the 1T-MoS_2@C_3N_4 NR composites implies that the recombination rate of electrons and holes has been reduced, thereby contributing to the enhanced photocatalytic efficiency and stability toward hydrogen production.

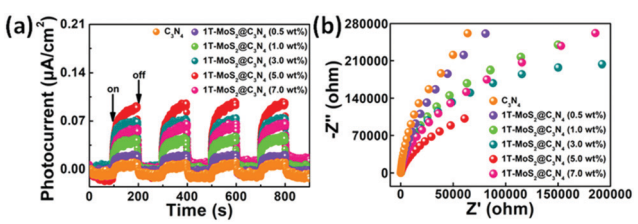

Fig. 9 (a) The transient photocurrent responses and (b) the electrochemical impedance spectra (EIS) of the samples under solar light irradiation.

The photocatalytic activity for H_2 evolution was evaluated under simulated sunlight irradiation using a 300 W Xe arc lamp with an AM-1.5 filter. Fig. 10 presents a comparison of the photocatalytic H_2 production activities of C_3N_4 NRs (Pt as co-catalyst) and 1T-MoS_2@C_3N_4 NR composites containing different amounts of co-catalyst (0.5, 1.0, 3.0, 5.0 and 7.0 wt% 1T-MoS_2 QDs) in aqueous solution with TEOA. It can be seen that no H_2 is detected for C_3N_4 NRs in the absence of a co-catalyst (Fig. S8, ESI†), which can be ascribed to their limited light-harvesting efficiency and fast recombination of photoinduced charge carriers. Notably, after the assembly of 1T-MoS_2 QDs, a significantly improved photocatalytic performance was observed, with the highest photocatalytic H_2 evolution rate of 565 μmol h^{-1} g^{-1} occurring for the 5.0 wt% MoS_2 sample (Fig. 10). The 1T-MoS_2@C_3N_4 NR composites (0.5, 1.0 and 3.0 wt%), which are composed of a small amount of MoS_2, display a lower photocatalytic performance compared with 1T-MoS_2@C_3N_4 NR composites (5.0 wt%), because of the relatively poor light absorption (Fig. 7). Furthermore, with increasing the content of MoS_2 from 5.0 wt% to 7.0 wt%, a decrease in the photocatalytic activity of the 1T-MoS_2@C_3N_4 NR composites is discovered, which is due to the light-screening effect of the excessive amount of co-catalysts.[59,60]

Besides, the photocatalytic H_2 evolution rate of 1T-MoS_2@C_3N_4 NR composites (5.0 wt%) also exceeds that of Pt@C_3N_4

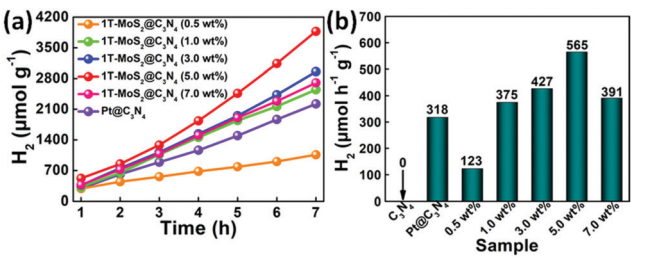

Fig. 10 (a) Cumulated evolution and (b) photocatalytic H_2 evolution rate of C_3N_4 NRs ($H_2PtCl_6{\cdot}6H_2O$ as co-catalyst) and 1T-MoS_2@C_3N_4 NR composites containing different amounts of co-catalyst (0.5, 1.0, 3.0, 5.0 and 7.0 wt% 1T-MoS_2 QDs) under simulated solar light.

NRs (318 μmol h^{-1} g^{-1}). Moreover, the photocatalytic H_2 production catalyzed by 1T-MoS_2@C_3N_4 NR composites (5.0 wt%) is measured under prolonged simulated solar light irradiation for 21 h (Fig. S9, ESI†), and no obvious decay of photocatalytic HER is discerned, suggesting good durability and practical application for 1T-MoS_2@C_3N_4 NR composites. High-resolution peak-fitting XPS spectra of Mo 3d of 1T-MoS_2@C_3N_4 NR composites (5.0 wt%) after cycling under simulated solar light irradiation are measured (Fig. S10, ESI†). As shown in Fig. S10 (ESI†), there is almost no change in the Mo^{6+} (MoO_3) XPS peaks of the 1T-MoS_2@C_3N_4 NR composites (5.0 wt%) before cycling and after cycling, which further confirms the excellent stability of the 1T-MoS_2@C_3N_4 NR composites. We further evaluated the apparent quantum efficiency (AQE) of the samples under a 300 W Xe arc lamp with an AM-1.5 optical filter. Table S2 (ESI†) shows the comparison of AQE values over C_3N_4 NRs, Pt@C_3N_4 NRs and 1T-MoS_2@C_3N_4 NR composites containing different amounts of 1T-MoS_2 QDs (0.5, 1.0, 3.0, 5.0 and 7.0 wt%): 0 (C_3N_4 NRs) < 0.47% (1T-MoS_2@C_3N_4-0.5 wt%) < 0.99% (Pt@C_3N_4 NRs) < 1.13% (1T-MoS_2@C_3N_4-1.0 wt%) < 1.21% (1T-MoS_2@C_3N_4-7.0 wt%) < 1.31% (1T-MoS_2@C_3N_4-3.0 wt%) < 1.73% (1T-MoS_2@C_3N_4-5.0 wt%). Therefore, the 1T-MoS_2@C_3N_4 NR composites can be used as an efficient and stable photocatalyst.

To further explore the photocatalytic mechanism of 1T-MoS_2@C_3N_4 NR composites, Mott–Schottky plots were recorded to evaluate the conduction band (CB) levels of C_3N_4 NRs. As shown in Fig. S11 (ESI†), by extrapolating the x intercept of the linear region, the flat band potentials (E_{FB}) of C_3N_4 NRs were obtained to be −0.71 V *vs.* Ag/AgCl from the Mott–Schottky plots, corresponding to −0.51 V *vs.* the normal hydrogen electrode (NHE). It is widely accepted that the conduction band potential (E_{CB}) of an n-type semiconductor is more negative by about 0.1 V than its E_{FB} value,[61] therefore, the E_{CB} of C_3N_4 NRs could be approximated to be −0.61V *vs.* NHE. Combined with the E_g of C_3N_4 NRs (1.38 eV) obtained from the UV-vis DRS spectra (Fig. S6b, ESI†), the estimated valence band potential (E_{VB}) of C_3N_4 NRs is 0.77 eV *vs.* NHE.

Based on the above results, a possible photocatalytic HER process of 1T-MoS_2@C_3N_4 NR composites under simulated solar light irradiation is proposed and schematically displayed in Scheme 4. Typically, under simulated solar light irradiation, electron–hole pairs are generated in C_3N_4 NRs, and then the photo-excited electrons rapidly transfer to the 1T-MoS_2 QD co-catalyst quickly, because the 1T-MoS_2 QDs are good electron acceptors due to their metallic characteristics. As photoelectron acceptors, 1T-MoS_2 QDs act as active sites for H_2 evolution. In addition, in the 1T-MoS_2@C_3N_4 NR composites, small-sized 1T-MoS_2 QDs well attached on the C_3N_4 NRs enable electron transfer from C_3N_4 NRs to 1T-MoS_2 QDs in a short distance and simultaneously provide more reaction sites on both basal planes and edges for the evolution of H_2. The holes would react with the sacrificial agent (TEOA) (Scheme 4). This effective electron transport between C_3N_4 NRs and 1T-MoS_2 QDs tremendously decreases the recombination of electron–hole pairs and prolong the charge lifetime.

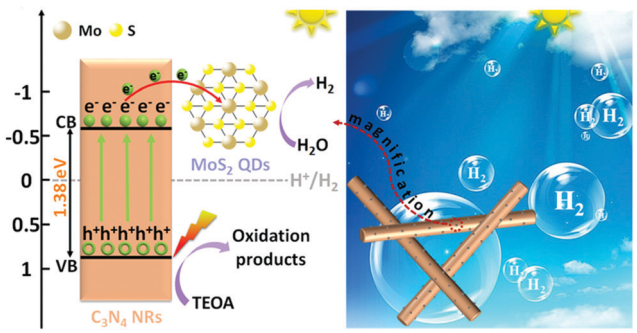

Scheme 4 Schematic illustration of the photocatalytic mechanism of 1T-MoS_2@C_3N_4 NR composites under simulated solar light irradiation.

4. Conclusions

1T-MoS_2 QDs were successfully synthesized and subsequently assembled with C_3N_4 NRs as effective co-catalysts for photocatalytic H_2 evolution over noble metal Pt. Specifically, an optimized 1T-MoS_2@C_3N_4 NR composite (5.0 wt%) attains a remarkable increased solar light photocatalytic H_2 evolution rate of 565 μmol h^{-1} g^{-1} which is apparently higher than that of Pt@C_3N_4 NRs (318 μmol h^{-1} g^{-1}). The highly efficient photocatalytic performance of the 1T-MoS_2@C_3N_4 NR composite is primarily attributed to the following facts: (1) 1T-MoS_2 QDs in cooperation with C_3N_4 NRs can enhance the light absorption intensity and broaden the light absorption range to NIR light; (2) the tiny particle size of 1T-MoS_2 QD co-catalysts can provide more active sites, which is helpful for the photocatalytic reaction; (3) the close contact layer between metallic 1T-MoS_2 QDs and C_3N_4 NRs is more favorable to transfer photo-generated electrons from the CB of C_3N_4 to the surface of conductive 1T-MoS_2, and then the electrons would rapidly participate in photocatalytic HER.

Conflicts of interest

There are no conflicts to declare.

Acknowledgements

The authors are thankful for funding from the National Natural Science Foundation of China (No. 51872173), Taishan Scholarship of Young Scholars (No. tsqn201812068), Natural Science Foundation of Shandong Province (No. ZR2017JL020), Taishan Scholarship of Climbing Plan (No. tspd20161006), and the Key Research and Development Program of Shandong Province (No. 2018GGX102028).

Notes and references

1 Y. Cheng, G. Yang, H. Jiang, S. G. Zhao, Q. Liu and Y. Xie, *ACS Appl. Mater. Interfaces*, 2018, **10**, 38880–38891.
2 Y. Ma, L. Yin, G. Cao, Q. Huang, M. He, W. Wei, H. Zhao, D. Zhang, M. Wang and T. Yang, *Small*, 2018, 1703613.
3 Y. Wang, W. Wei, X. Liu and Y. Gu, *Sol. Energy Mater. Sol. Cells*, 2012, **98**, 129–145.

4 X. Li, X. Lv, N. Li, J. Wu, Y. Z. Zheng and X. Tao, *Appl. Catal., B*, 2019, **243**, 76–85.
5 X. Zhang, Y. Guo, J. Tian, B. Sun, Z. Liang, X. Xu and H. Cui, *Appl. Catal., B*, 2018, **232**, 355–364.
6 M. Zhu, S. Kim, L. Mao, M. Fujitsuka, J. Zhang, X. Wang and T. Majima, *J. Am. Chem. Soc.*, 2017, **139**, 13234–13242.
7 H. Zhang, G. Liu, L. Shi, H. Liu, T. Wang and J. Ye, *Nano Energy*, 2016, **22**, 149–168.
8 H. Li, X. Zhao, H. Liu, S. Chen, X. Yang, C. Lv, H. Zhang, X. She and D. Yang, *Small*, 2018, 1802824.
9 L. Hang, T. Zhang, Y. Sun, D. Men, X. Lyu, Q. Zhang, W. Cai and Y. Li, *J. Mater. Chem. A*, 2018, **6**, 19555–19562.
10 P. Li, X. Duan, Y. Kuang, Y. Li, G. Zhang, W. Liu and X. Sun, *Adv. Energy Mater.*, 2018, **8**, 1703341.
11 W. Zhang, Y. Zou, H. Liu, S. Chen, X. Wang, H. Zhang, X. She and D. Yang, *Nano Energy*, 2019, **56**, 813–822.
12 Y. Li, Z. Yin, G. Ji, Z. Liang, Y. Xue, Y. Guo, J. Tian, X. Wang and H. Cui, *Appl. Catal., B*, 2019, **246**, 12–20.
13 Y.-N. Liu, C.-C. Shen, N. Jiang, Z.-W. Zhao, X. Zhou, S.-J. Zhao and A.-W. Xu, *ACS Catal.*, 2017, **7**, 8228–8234.
14 Y. Tan, Z. Shu, J. Zhou, T. Li, W. Wang and Z. Zhao, *Appl. Catal., B*, 2018, **230**, 260–268.
15 D. Zeng, T. Zhou, W.-J. Ong, M. Wu, X. Duan, W. Xu, Y. Chen, Y.-A. Zhu and D.-L. Peng, *ACS Appl. Mater. Interfaces*, 2019, **11**, 5651–5660.
16 Y. Cui, Z. Ding, X. Fu and X. Wang, *Angew. Chem., Int. Ed.*, 2012, **124**, 11984–11988.
17 Y. Li, Y. Xue, J. Tian, X. Song, X. Zhang, X. Wang and H. Cui, *Sol. Energy Mater. Sol. Cells*, 2017, **168**, 100–111.
18 D. Zeng, W. Xu, W.-J. Ong, J. Xu, H. Ren, Y. Chen, H. Zheng and D.-L. Peng, *Appl. Catal., B*, 2018, **221**, 47–55.
19 Y. Chang, Z. Li, X. Shen, B. Zhu, D. K. Macharia, Z. Chen and L. Zhang, *J. Hazard. Mater.*, 2018, **344**, 1188–1197.
20 H.-J. Li, D.-J. Qian and M. Chen, *ACS Appl. Mater. Interfaces*, 2015, **7**, 25162–25170.
21 K. Chang, X. Hai, H. Pang, H. Zhang, L. Shi, G. Liu, H. Liu, G. Zhao, M. Li and J. Ye, *Adv. Mater.*, 2016, **28**, 10033–10041.
22 D. Lu, H. Wang, X. Zhao, K. K. Kondamareddy, J. Ding, C. Li and P. Fang, *ACS Sustainable Chem. Eng.*, 2017, **5**, 1436–1445.
23 N. Qina, J. Xiong, R. Lianga, Y. Liu, S. Zhang, Y. Li, Z. Li and L. Wu, *Appl. Catal., B*, 2017, **202**, 374–380.
24 X.-L. Yin, L.-L. Li, W.-J. Jiang, Y. Zhang, X. Zhang, L.-J. Wan and J.-S. Hu, *ACS Appl. Mater. Interfaces*, 2016, **8**, 15258–15266.
25 Y. Jiang, X. Li, S. Yu, L. Jia, X. Zhao and C. Wang, *Adv. Funct. Mater.*, 2015, **25**, 2693–2700.
26 Y. Li, H. Wang, L. Xie, Y. Liang, G. Hong and H. Dai, *J. Am. Chem. Soc.*, 2011, **133**, 7296–7299.
27 H. Xu, S. Liu, Z. Ding, S. J. R. Tan, K. M. Yam, Y. Bao, C. T. Nai, M.-F. Ng, J. Lu, C. Zhang and K. P. Loh, *Nat. Commun.*, 2016, **7**, 12904.
28 C. Ling, Y. Ouyang, L. Shi, S. Yuan, Q. Chen and J. Wang, *ACS Catal.*, 2017, **7**, 5097–5102.
29 J. M. Wu, W. E. Chang, Y. T. Chang and C. K. Chang, *Adv. Mater.*, 2016, **28**, 3718–3725.
30 X. Lu, Y. Lin, H. Dong, W. Dai, X. Chen, X. Qu and X. Zhang, *Sci. Rep.*, 2017, **7**, 42309.
31 C. Liu, L. Wang, Y. Tang, S. Luo, Y. Liu, S. Zhang, Y. Zeng and Y. Xu, *Appl. Catal., B*, 2015, **164**, 1–9.
32 W. Zhou, Z. Yin, Y. Du, X. Huang, Z. Zeng, Z. Fan, H. Liu, J. Wang and H. Zhang, *Small*, 2013, **9**, 140–147.
33 X. Hao, Z. Jin, H. Yang, G. Lu and Y. Bi, *Appl. Catal., B*, 2017, **210**, 45–56.
34 D. Gopalakrishnan, D. Damien and M. M. Shaijumon, *ACS Nano*, 2014, **8**, 5297–5303.
35 W. Gu, Y. Yan, C. Zhang, C. Ding and Y. Xian, *ACS Appl. Mater. Interfaces*, 2016, **8**, 11272–11279.
36 G. Eda, H. Yamaguchi, D. Voiry, T. Fujita, M. Chen and M. Chhowalla, *Nano Lett.*, 2011, **11**, 5111–5116.
37 U. Maitra, U. Gupta, M. De, R. Datta, A. Govindaraj and C. N. R. Rao, *Angew. Chem., Int. Ed.*, 2013, **125**, 13295–13299.
38 D. Voiry, M. Salehi, R. Silva, T. Fujita, M. Chen, T. Asefa, V. B. Shenoy, G. Eda and M. Chhowalla, *Nano Lett.*, 2013, **13**, 6222–6227.
39 Q. Li, Q. Shang, A. Khalil, Q. Fang, S. Chen, Q. He, T. Xiang, D. Liu, Q. Zhang, Y. Luo and L. Song, *ChemCatChem*, 2016, **8**, 1–7.
40 D. Ruan, S. Kim, M. Fujitsuka and T. Majima, *Appl. Catal., B*, 2018, **238**, 638–646.
41 S. Martha, A. Nashim and K. M. Parida, *J. Mater. Chem. A*, 2013, **1**, 7816–7824.
42 L. Kong, Y. Ji, Z. Dang, J. Yan, P. Li, Y. Li and S. Liu, *Adv. Funct. Mater.*, 2018, **28**, 1800668.
43 X. L. Yin, L. L. Li, W. J. Jiang, Z. Yun, Z. Xiang, L. J. Wan and J. S. Hu, *ACS Appl. Mater. Interfaces*, 2016, **8**, 15258.
44 M. Liu, F. Li, Z. Sun, L. Ma, L. Xu and Y. Wang, *Chem. Commun.*, 2014, **50**, 11004–11007.
45 W.-J. Ong, L. K. Putri, L.-L. Tan, S.-P. Chai and S.-T. Yong, *Appl. Catal., B*, 2016, **180**, 530–543.
46 A. Thomas, A. Fischer, F. Goettmann, M. Antonietti, J. Müller, R. Schlçgl and J. M. Carlsson, *J. Mater. Chem.*, 2008, **18**, 4893.
47 Y. Chang, Z. Liu, X. Shen, B. Zhu, D. K. Macharia, Z. Chen and L. Zhang, *J. Hazard. Mater.*, 2018, **344**, 1188–1197.
48 J. Li, Y. Yin, E. Liu, Y. Ma, J. Wan, J. Fan and X. Hu, *J. Hazard. Mater.*, 2017, **321**, 183–192.
49 M. A. Lukowski, A. S. Daniel, F. Meng, A. Forticaux, L. Li and S. Jin, *J. Am. Chem. Soc.*, 2013, **135**, 10274–10277.
50 Q. Liu, Q. Fang, W. Chu, Y. Wan, X. Li, W. Xu, M. Habib, S. Tao, Y. Zhou, D. Liu, T. Xiang, A. Khalil, X. Wu, M. Chhowalla, P. M. Ajayan and L. Song, *Chem. Mater.*, 2017, **29**, 4738–4744.
51 N. Li, J. Zhou, Z. Sheng and W. Xiao, *Appl. Surf. Sci.*, 2018, **430**, 218–224.
52 X. Ren, L. Pang, Y. Zhang, X. Ren, H. Fan and S. Liu, *J. Mater. Chem. A*, 2015, **3**, 10693–10697.
53 X. Geng, W. Sun, W. Wu, B. Chen, A. Al-Hilo, M. Benamara, H. Zhu, F. Watanabe, J. Cui and T. P. Chen, *Nat. Commun.*, 2016, **7**, 10672.
54 Z. Liang, X. Bai, P. Hao, Y. Guo, Y. Xue, J. Tian and H. Cui, *Appl. Catal., B*, 2019, **243**, 711–720.
55 Y. Li, X. Deng, J. Tian, Z. Liang and H. Cui, *Appl. Mater. Today*, 2018, **13**, 217–227.

56 B. Han, S. Liu, N. Zhang, Y. J. Xu and Z. R. Tang, *Appl. Catal., B*, 2017, **202**, 298–304.
57 A. Meng, J. Zhang, D. Xu, B. Cheng and J. Yu, *Appl. Catal., B*, 2016, **198**, 286–294.
58 X. Hu, S. Lu, J. Tian, N. Wei, X. Song, X. Wang and H. Cui, *Appl. Catal., B*, 2019, **24**, 329–337.
59 L. Shen, M. Luo, Y. Liu, R. Liang, F. Jing and L. Wu, *Appl. Catal., B*, 2015, **166–167**, 445–453.
60 Y. Hou, A. B. Laursen, J. Zhang, G. Zhang, Y. Zhu, X. Wang, S. Dahl and I. Chorkendorff, *Angew. Chem., Int. Ed.*, 2013, **125**, 3709–3713.
61 T. N. Trung, D. B. Seo, N. D. Quang, D. Kim and E. T. Kim, *Electrochim. Acta*, 2018, **260**, 150–156.

